

# Effects of compositional variation on the thermal stability of $\theta'$ -Al<sub>2</sub>Cu precipitates and elevated-temperature strengths in Al-Cu 206 alloys

Jovid Rakhmonov<sup>a,\*</sup>, Kun Liu<sup>a,\*\*</sup>, X. Grant Chen<sup>a</sup>

<sup>a</sup>Department of Applied Science, University of Quebec at Chicoutimi, Saguenay, Quebec, QC, G7H 2B1, Canada

\* Corresponding author: J. Rakhmonov (jovid.rakhmonov1@uqac.com)

\*\* Corresponding author: K. Liu (kun.liu@uqac.com)

## Abstract

This study explored the effects of compositional variation of Al-Cu 206 alloys (Si and Mn concentrations, 0.12 wt.% each vs. 0.3 wt.% each) on the precipitation and thermal stability of  $\theta'$  precipitates, and the associated elevated-temperature strengths during long-term thermal exposure at 300 °C. The results indicated that both alloys under the T7 condition exhibited comparable yield strengths (YSs) at 20 and 300 °C, which were predominantly controlled by  $\theta'$  precipitates. Upon exposure at 300 °C for up to 1000 h, the  $\theta'$  precipitates in the alloy with low Si and Mn concentrations remained stable and resistant to transformation into the equilibrium  $\theta$  phase. However, the coarsening of  $\theta'$  was locally anisotropic along  $\langle 100 \rangle_{\text{Al}}$  directions and proceeded through both lengthening and thickening, resulting in the continuing decline in YS at 300 °C from 93 MPa after 300°C/100h to 78 MPa after 300°C/1000h. Conversely, the  $\theta'$  precipitates in the alloy with high Si and Mn concentrations underwent almost complete transformation into deleterious  $\theta$  after only 100 h at 300 °C, thus imparting a significantly lower YS of 69 MPa after 300°C/100h. The possible sources of these microstructure and property changes with the compositional variation were explored. This study has implications for strategic design of Al-Cu alloys for high-temperature applications.

## Keywords

Al-Cu 206 alloys; Precipitation kinetics;  $\theta'$ -Al<sub>2</sub>Cu precipitates; Coarsening; High-temperature strength;

## 1. Introduction

Owing to their high strength-to-weight ratio, the Al-Cu alloys are increasingly being used for the fabrication of thermally critical structural components, such as engine blocks, cylinder heads, and pistons, in the automobile industry, which operate at elevated temperatures [1-3]. Effective functionality at higher temperature and stress conditions is one of the key parameters required of the new generation powertrain components [4,5]. The operating temperature has been continuously increasing with the development of more efficient internal combustion engines, and it is expected to increase further to 300–350 °C in the near future [4,5]. This implies the necessity for durable aluminum alloys that preserve robust elevated-temperature mechanical properties after long-term thermal and thermo-mechanical exposure during service. However, when exposed to temperatures exceeding 200 °C, the high strength Al-Cu alloys, which are predominantly strengthened by a large number of nanoscale metastable  $\theta'$  precipitates, display a rapid

decline in mechanical properties [5-7]. This is primarily attributed to the coarsening of  $\theta'$  precipitates and their transformation as the exposure temperature and time increase [5,6,8].

Recent studies have garnered increased interest in the stabilization of  $\theta'$  precipitates in Al-Cu alloys at even higher temperatures via alloying with some transition metals [9-16]. It has been reported that Zr, Mn, and Sc were beneficial for the thermal stability of  $\theta'$  precipitates through their segregation to  $\theta'/\alpha$ -Al interfaces, which significantly improved the elevated-temperature mechanical properties [9,11,14,15,17]. Our research group recently demonstrated that in the presence of Zr, V, and Ti, as well as an optimum amount of Mg in Al-Cu 224 alloys, the  $\theta'$  precipitates formed during the aging treatment remained stable and resistant to coarsening during thermal exposure at 300 °C for up to 1000 h [13]. However, adding transition metals does not appear to provide similar stabilizing effects on the  $\theta'$  precipitates in Al-Si-Cu alloys, e.g., 319, in which the  $\theta'$  precipitates are the dominant strengtheners as well [5,18]. This is likely due to the presence of Si in the Al-Si-Cu alloys that accelerates the  $\theta'$  to  $\theta$  transformation [19,20]. Although Si is an important alloying element in most Al-Cu alloys [21,22], it is not yet clear what Si concentration could influence the thermal stability and coarsening behavior of  $\theta'$  precipitates in Al-Cu alloys during long-term thermal exposure at 300 °C.

The presence of a certain amount of Si in combination with Mn in Al-Cu 206 alloys has also been reported to be an effective approach for minimizing the deleterious influence of Fe [23]. However, this approach necessitates the addition of relatively higher concentrations of both Si and Mn to the alloy than the amounts typically in Al-Cu 206 alloys [23]. Although Mn in combination with Zr has been found to increase the stability of  $\theta'$  phase to higher temperatures [11,24], its  $\theta'$ -strengthening effect in the presence of Si in Al-Cu alloys has not been revealed yet.

Among the various alloys in the Al-Cu system, the 206 cast alloys are widely used for the manufacture of critical automotive and aerospace structural components [23]. Recent studies have shown that, with the exposure of T7-treated 206 alloy at 300 °C for 200 h, almost a complete transformation of  $\theta'$  precipitates into equilibrium  $\theta$  phase occurred in the microstructure, rendering the alloy with a significantly lower yield strength at 300 °C (56–60 MPa) [11,24] compared to the YSs of 105–140 MPa at 300 °C of similar 240-T7 and 224-T7 cast alloys [13]. The present study aims to investigate the effects of Si and Mn concentrations on the precipitation of  $\theta'$ -Al<sub>2</sub>Cu precipitates in Al-Cu 206 alloys during aging treatment, their thermal stability, and the evolutions of their associated elevated-temperature strengths during long-term thermal exposure at 300 °C.

## 2. Experimental Methodology

Two Al-Cu 206 alloys were investigated in the present study. The chemical compositions of the experimental alloys, analyzed using optical emission spectroscopy, are listed in Table 1. For simplicity, the alloys with low and high Si/Mn concentrations are referred to as the 206-L and 206-H alloys, respectively. The concentrations of Ti were obtained through the addition of Al-5Ti-1B grain refining master alloys to the molten metal. The standard ASTM B-108 permanent mold was used to produce the cast bars of the experimental alloys. The melt preparation and casting process were explained in detail in Ref. [23]. The average grain size was measured as ~ 130  $\mu$ m for both alloys using linear intercept method.

The cast samples were heat-treated in an electrical air-circulating furnace to obtain the T7 temper. It consisted of a solution treatment at 520 °C for 10 h, followed by water quenching to room temperature. The artificial aging was executed at 185 °C for 5 h. To investigate the microstructural and mechanical responses of the T7-treated alloys during high-temperature exposure, the samples were held at 300 °C for three different times: 100, 500, and 1000 h, hereafter referred to as 300°C/100h, 300°C/500h and 300°C/1000h exposures, respectively.

Microstructural characterization of the alloys was performed using scanning electron microscopy (SEM) and transmission electron microscopy (TEM). Specimen preparation for the microstructure observations under SEM was conducted using standard metallographic techniques. The TEM specimen was prepared by punching a thin sample that was 3 mm in diameter and ~400  $\mu$ m thick, followed by reducing

the sample thickness to  $\sim 50 \mu\text{m}$  via grinding and polishing. It was finalized by twin-jet electrochemical polishing in a solution consisting of 67% methanol and 33% nitric acid. The voltage in the twin-jet equipment was set at 20 V, and the temperature of the solution was maintained between  $-20$  and  $-30 \text{ }^\circ\text{C}$ . The microstructure observations using TEM were performed under the g200 beam condition. The two-beam convergent beam diffraction pattern was used to measure the thickness of the TEM specimen in the observed field. To qualitatively assess the level of solute enrichment in the  $\alpha$ -Al matrix, electrical conductivity tests were performed using a Sigmascope SMP10 unit at a frequency of 60 kHz.

The mechanical performance of the experimental alloys was characterized by conducting compressive yield strength tests and Vickers microhardness tests. A Gleeble 3800 thermo-mechanical simulator unit was used to measure the yield strength at 20 and  $300 \text{ }^\circ\text{C}$ . The compression tests were conducted on specimens that were 10 mm in diameter and 15 mm in height at a strain rate of  $10^{-3} \text{ s}^{-1}$  until a total strain of 0.2 was reached. Several specimens (at least three) were used per condition for the compression tests. Vickers microhardness testing was executed under a load of 100 g and dwell time of 20 s.

### 3. Results and Discussion

#### 3.1. As-cast and solutionized microstructures

Characterization of as-cast and solutionized microstructures is of importance because the precipitation of  $\theta'$  precipitates during the aging heat treatment is influenced by the alloying elements and solute content in the  $\alpha$ -Al matrix [13,25]. **Fig. 1a,b** show the typical as-cast microstructures of the experimental alloys. The microstructure of the 206-L alloy was composed of  $\alpha$ -Al dendrite cells, needle-like  $\text{Al}_7\text{Cu}_2\text{Fe}$  intermetallics, and the eutectic  $\text{Al}_2\text{Cu}$  phase (**Fig. 1a**). In contrast, the script-like  $\text{Al}_{15}(\text{FeMn})_3\text{Si}_2$  intermetallic, eutectic  $\text{Al}_2\text{Cu}$  and  $\text{Mg}_2\text{Si}$  phases, were found in 206-H alloy (**Fig. 1b**). Clearly, the high Mn and Si concentrations in the 206-H alloy promoted the formation of script-like  $\text{Al}_{15}(\text{FeMn})_3\text{Si}_2$  instead of needle-like  $\text{Al}_7\text{Cu}_2\text{Fe}$ . Moreover, increasing the Si content in the 206-H alloy caused the formation of a trace amount of  $\text{Mg}_2\text{Si}$  particles during solidification (**Fig. 1b**).

During the solution treatment, the majority of eutectic  $\text{Al}_2\text{Cu}$  particles in two alloys underwent dissolution into the  $\alpha$ -Al matrix, while both  $\text{Al}_7\text{Cu}_2\text{Fe}$  and  $\text{Al}(\text{FeMn})\text{Si}$  intermetallics remained undissolved (**Fig. 1c,d**). Few  $\text{Mg}_2\text{Si}$  particles in 206-H alloy experienced complete dissolution in the matrix. A qualitative comparison of the amount of undissolved  $\text{Al}_2\text{Cu}$  particles reveals that there were slightly more particles in the 206-H alloy than in the 206-L alloy.

To verify the stable phases and to estimate the solute concentration in the matrix, the thermodynamic equilibrium analyses at  $520 \text{ }^\circ\text{C}$  were conducted using Thermo-Calc software with TCAL 4 database, considering the sufficiently long solution time (10 h). The results are presented in Table 2, which indicate that the  $\alpha$ -Al and  $\text{Al}_7\text{Cu}_2\text{Fe}$  phases are the stable phases in 206-L alloy, whereas in 206-H alloy these are  $\alpha$ -Al,  $\text{Al}(\text{FeMn})\text{Si}$  and  $\text{Al}_2\text{Cu}$  phases after solutionized at  $520 \text{ }^\circ\text{C}$ . The results from Thermo-Calc calculation also imply that the Cu concentrations in the  $\alpha$ -Al matrix of both alloys are similar. The types of phases predicted by thermodynamic analyses are in reasonably good agreement with the microstructural observations (**Fig. 1c,d**). The presence of slightly more undissolved  $\text{Al}_2\text{Cu}$  in 206-H can be attributed to the fact that certain amount of Cu in 206-L alloy were consumed by insoluble Cu-rich  $\text{Al}_7\text{Cu}_2\text{Fe}$  intermetallics formed during solidification (**Fig. 1c**). From the estimated solute concentrations of  $\alpha$ -Al matrices of two alloys (

), it can be deduced that higher Si and Mn in 206-H alloy could also result in the higher supersaturation in its matrix upon solutionizing of this alloy compared to 206-L alloy. This is consistent with the EC and microhardness measurements of both alloys after solution treatment (see Table ). Lower EC value and higher microhardness for 206-H alloy indicates a higher degree of solute supersaturation in 206-H. The  $\alpha$ -Al matrix of 206-H becomes more supersaturated with Si and Cu.

### 3.2. Mechanical strength and microstructure under the T7 condition

The compressive yield strengths (YSs) at room temperature of the experimental alloys in the T7 state is shown in Fig. 2. Both alloys had a similar YS, although the 206-H alloy possessed a slightly higher YS than the 206-L alloy (~398 vs. 392 MPa). The room-temperature tensile properties of alloys with the same composition as 206-L and 206-H have been studied in [23]; it was reported that the ultimate tensile strength (UTS) and YS of the 206-L alloy under the T7 condition were 454 and 413 MPa, while the UTS and YS of the 206-H alloy were 461 and 423 MPa, respectively. For a given alloy, although a slight difference exists between the compressive and tensile YSs, which might be due to the different loading paths used in these studies, the results from both studies confirm that the room-temperature mechanical strengths of both alloys are very close.

The compressive YSs at 300 °C of the experimental alloys in T7 state are also shown in Fig. 2. Clearly, the Al-Cu 206 alloys experienced a significant reduction in their YSs compared to those at room temperature. The 206-L alloy possessed a YS of ~160 MPa at 300 °C, while the 206-H alloy had a YS of ~172 MPa. Similar to the room-temperature properties, the 206-H alloy possessed a moderately higher YS at 300 °C than the 206-L alloy.

Because precipitation hardening is the major strengthening mechanism in Al-Cu alloys [13], the precipitates formed during the aging treatment were studied using TEM. The typical microstructure of the 206-L alloy is shown in Fig. 3a, exhibiting a great number of nanoscale precipitates with a uniform length distribution. The corresponding selected area diffraction pattern (SADP) reveals the spots (Fig. 3b) that are the characteristic feature of the  $\theta'$ -Al<sub>2</sub>Cu phase [30]. The average thickness and length of  $\theta'$  precipitates were measured as 3.6 and 46 nm, respectively (Table 3). In addition to the predominant  $\theta'$  phase, a few cubic fine precipitates were observed (Fig. 3a), which were identified as  $\sigma$  (Al<sub>5</sub>Cu<sub>6</sub>Mg<sub>2</sub>) phase based on their morphology and the TEM-EDS results (Table 4) [16,31].

The microstructure of the 206-H alloy was also composed of the predominant  $\theta'$  precipitates (Fig. 3c, d). However, the  $\theta'$  precipitates, with an average thickness and length of 3.9 and 55 nm, respectively, exhibited a comparably less uniform length distribution, which is also evidenced by the remarkably larger standard error of the average length compared to those in the 206-L alloy (Table 3). Correspondingly, the  $\theta'$  precipitates appeared less dense in the 206-H alloy relative to the 206-L alloy (1812 vs. 2197  $\mu\text{m}^{-3}$ ). In addition to the  $\theta'$  precipitates, numerous dark spots were observed in the microstructure of the 206-H alloy (Fig. 3c). These spots are thought to be the cross-sections of needle-like  $\beta''$ -MgSi precipitates formed along  $\langle 001 \rangle_{\text{Al}}$  directions [32]. The diameter of the dark spots was approximated at 4 nm, which is in the typical range of the cross-sectional diameter of  $\beta''$ -MgSi precipitates [33,34].

As for the strengthening contribution under the T7 condition, the room-temperature YSs of both alloys were undoubtedly governed primarily by the  $\theta'$  precipitates.  $\theta'$  is well known as the primary strengthening phase in Al-Cu alloys, contributing to the strengthening by the Orowan looping mechanism [13,32,35]. The  $\beta''$  phase observed in the 206-H alloy (see Fig. 3) is known as an effective alloy strengthener in Al-Cu-Mg and Al-Mg-Si alloys [8]. The  $\beta''$  phase, owing to its needle-like morphology, requires relatively lower concentrations of alloying elements, i.e., Mg and Si, in the alloy compared to the platelet-shaped precipitates to provide similar levels of strengthening [32]. Moreover, the  $\theta'$  and  $\beta''$  precipitates in the microstructure of the 206-H alloy did not appear to overlap, which produces low interparticle spacing and thus a better strengthening effect [32]. Although a lower number density of  $\theta'$  precipitates was observed in the 206-H alloy compared to the 206-L alloy (see Table 3), the presence of additional  $\beta''$  precipitates as a minor phase in the former alloy gave this alloy a relatively higher strength compared to the 206-L alloy.

A significant reduction in the YS of both alloys at 300 °C (see Fig. 2) is primarily attributed to the thermally activated dislocation motion through climb and cross-slip, which become increasingly effective at high temperature [36]. Because the compression tests at 300 °C for the T7 samples were completed within a few minutes owing to the quick resistance heating in the Gleeble unit, microstructural changes of the strengthening precipitates are thought to be negligible, and therefore, the  $\theta'$  or the co-existence of  $\theta'$  and  $\beta''$  precipitates in both alloys still controlled the strengths measured at 300 °C. Similar to the trend in

the room-temperature YS, the 206-H alloy showed a moderately higher YS at 300 °C relative to the 206-L alloy.

### ***3.3. Elevated-temperature strengths and thermal stability of $\theta'$ precipitates during long-term thermal exposure***

To evaluate the effect of compositional variation on the elevated-temperature strength during long-term thermal exposure, the samples, after the T7 treatment, were thermally exposed at 300 °C for 100, 500, and 1000 h, and the compressive YSs of these samples were measured at 300 and 20 °C. As shown in Fig. 4a, the YSs at 300 °C of the 206-L and 206-H alloys after the 300 °C/100 h exposure were 93 and 69 MPa, respectively, which are reduced by 67 MPa (40%) and 103 MPa (60%) compared with those obtained in the T7 state (Fig. 2). This indicates a significant reduction in the YSs at 300 °C of both alloys after the 300 °C/100 h exposure relative to the T7 state. With prolonged thermal exposure, both alloys showed a gradually declining YS at 300 °C. The YS at 300 °C of the 206-L alloy decreased from 93 MPa after 100 h to 86 MPa and finally to 78 MPa after 500 and 1000 h, respectively, while the YS at 300 °C of the 206-H alloy dropped from 69 MPa after 100 h to 66 MPa and further to 64 MPa after 500 and 1000 h, respectively. It is worth remarking here that the 206-L alloy after the 300°C/1000h exposure still possessed a higher YS at 300 °C than the 206-H alloy after the 300°C/100h exposure (78 vs. 64 MPa), indicating superior thermal stability of the former alloy over the latter.

Powertrain components generally encounter high thermal loads during start-stop cycles [2], where the room-temperature strengths of aluminum cast parts after a long thermal exposure period are also critical for the durability of the engines. It can be seen from Fig. 4b that the evolution of the YSs at 20 °C after prolonged thermal exposure reveals a similar trend to that observed at 300 °C (Fig. 4a). The YS at 20 °C of the 206-L alloy decreased from 150 MPa after the 300°C/100h exposure to 135 MPa and further to 119 MPa after the 300°C/500h and 300°C/1000h exposures, respectively. In contrast, the YS at 20 °C of the 206-H alloy decreased from 110 MPa after the 300°C/100h exposure to 104 MPa after the 300°C/1000h exposure. These results indicate that the 206-L alloy displays significantly higher YSs than the 206-H by 40 MPa (35%) after the 300°C/100h exposure and 15 MPa (14%) after the 300°C/1000h exposure.

Fig. 5a–c shows the typical TEM images and the corresponding SADP of the 206-L alloy after the 300°C/100h exposure. The microstructure is characterized by the presence of  $\theta'$  precipitates, appearing much coarser (15.3 nm in average thickness and 192 nm in average length, Fig. 5a, b and Table 5) than those observed under the T7 condition (Fig. 3a and Table 3). Coarsened  $\theta'$  precipitates, in turn, contributed less to the strengthening of the alloy [13,32,37], and therefore, a significantly lower elevated-temperature YS was obtained for the 206-L alloy after the 300°C/100h exposure (Fig. 4) than in the T7 state (**Fig. 2**).

Moreover, unlike in the T7 state (**Fig. 3a**), the  $\theta'$  precipitates after thermal exposure exhibited a fairly non-uniform distribution along the two edge-on  $\{200\}_{\text{Al}}$  planes resolved under the  $\langle 001 \rangle_{\text{Al}}$  zone axis (see Fig. 5a, b). The  $\theta'$  precipitates in the region indicated by the arrow in Fig. 5b were predominantly aligned along the  $[010]_{\text{Al}}$  direction, whereas most of the precipitates in the other regions in Fig. 5b were parallel to the  $[-100]_{\text{Al}}$  direction. The SADP in Fig. 5c corresponding to Fig. 5b also reveals a much higher intensity of diffraction spots representing  $\theta'$  precipitates on one of the two resolved edge-on  $\{200\}_{\text{Al}}$  planes compared with the other. These observations imply that the  $\theta'$  precipitates in a given local region, existing on a certain  $\{200\}_{\text{Al}}$  plane, predominantly undergo coarsening during thermal exposure, while the precipitates in that local region existing on the other  $\{200\}_{\text{Al}}$  planes tend to shrink and eventually vanish. Coarsening occurred through a further increase in the size of the larger precipitates at the expense of smaller precipitates, which is also called Ostwald ripening [3,38]. Moreover, the diffusion fields between the neighboring plate-shaped precipitates have been reported to exert significant influence on the tendency of precipitates to experience either coarsening or dissolution [39,40]. The interaction of the diffusion fields of neighboring precipitates lying along the same  $\{200\}_{\text{Al}}$  plane favors the coalescence of these precipitates to reduce the interfacial energy, whereas the same interaction between the neighboring precipitates lying along different  $\{200\}_{\text{Al}}$

planes restricts their coalescence [39,41]. These competing interactions and Ostwald ripening, taking place concurrently during coarsening, are thought to be responsible for such locally anisotropic coarsening of the  $\theta'$  precipitates along with the  $\langle 100 \rangle_{\text{Al}}$  directions during thermal exposure of the 206-L alloy. It is speculated that such locally anisotropic coarsening in a certain local region of an  $\alpha$ -Al grain commences through the coalescence of the precipitates in the  $\{200\}_{\text{Al}}$  plane that was most favorable for this process to occur, and the precipitates in the other two  $\{200\}_{\text{Al}}$  planes, which were in a comparably less favorable position for their coalescence, tended to shrink and eventually disappear as the radius of curvature of these precipitates soon became smaller than that of coalescing/coalesced precipitates.

After the prolonged 300°C/1000h exposure, no evidence of the  $\theta'$  to  $\theta$  transformation was observed in the 206-L alloy as the precipitates remained  $\theta'$  phase with platelet morphology (Fig. 5d, e) with spot reflections representing  $\theta'$  in the corresponding SADP (Fig. 5f). Hence, it can be implied that, although they have a locally non-uniform distribution along  $\{200\}_{\text{Al}}$  planes, the  $\theta'$  precipitates in the 206-L alloy remain stable during thermal exposure at 300 °C for long times. Moreover, coarsening of the  $\theta'$  precipitates during thermal exposure proceeded not only by lengthening, but also by thickening, as their average thickness increased from ~15.3 nm after 300°C/100h to ~18.5 nm after 300°C/1000h (Table 5), largely explaining why the YS at 300 °C of the 206-L alloy gradually decreased with prolonged thermal exposure because thickening, as opposed to lengthening, contributes more to the increase in interparticle spacing, and hence decrease in strength [42].

Fig. 6 shows the typical microstructure of the 206-H alloy after 300°C/100h exposure, which exhibited the principal equilibrium  $\theta$  ( $\text{Al}_2\text{Cu}$ ) phase with a small fraction of  $\theta'$  precipitates. The corresponding SADP also reveals weak faint spots representing the  $\theta'$  phase (Fig. 6c), indicating a largely reduced fraction of  $\theta'$  phase in this condition. In addition to the dominant  $\theta$  phase, some S ( $\text{Al}_2\text{CuMg}$ ) and  $\beta$  ( $\text{Mg}_2\text{Si}$ ) particles as minor phases, identified based on the TEM-EDS results (Table 6), were also observed in the microstructure (Fig. 6b).

Undoubtedly, the instability of  $\theta'$  and transformation from  $\theta'$  to  $\theta$  in the 206-H alloy during thermal exposure is responsible for the significantly lower YS compared to the 206-L alloy (Fig. 4) because the coarse equilibrium  $\theta$  phase has a negligible strengthening effect [43]. It is thus inferred that the dominant  $\theta'$  precipitates in the 206-L alloy after the 300°C/100h and even the 300°C/1000h exposures, as opposed to the  $\theta$ -dominated microstructure in the 206-H alloy after the 300°C/100h exposure, renders the former alloy higher strength after even 1000 h of exposure compared to the latter one after 100 h of exposure (Fig. 4). Undoubtedly, the few remaining  $\theta'$  precipitates in the 206-H alloy after the 300°C/100h exposure (Fig. 6a, b) underwent a complete transformation into equilibrium  $\theta$  during prolonged thermal exposure, slightly reducing the elevated-temperature YS of this alloy after 1000 h of exposure (Fig. 4).

### ***3.4. Comparison of the thermal stability and associated elevated-temperature strengths of various Al-Cu alloys***

As shown in Fig. 5, the  $\theta'$  precipitates remained relatively stable in the 206-L alloy even after the 300°C/1000h exposure. In recent studies [11,24], it was reported that the majority of the  $\theta'$  precipitates in an Al5CuMg 206-type alloy were transformed into undesirable equilibrium  $\theta$  phase after a 300°C/200h exposure. Correspondingly, the YS at 300 °C of this alloy after the 300°C/200h was approximately 60 MPa (Fig. 1 in [11,24]), which is remarkably lower than that of the 206-L alloy even after the 300°C/1000h exposure (Table 7). By comparison, it was found that the Al5CuMg alloy in [11,24] had almost the same chemical composition as the 206-L alloy in the present study except a much lower Ti concentration (0.02 wt.% vs. 0.21 wt.% in 206-L). Recently, it was discovered that Zr and Sc can exert beneficial effects on the thermal stability of  $\theta'$  precipitates through their segregation to  $\theta'/\alpha$ -Al interfaces and, hence, significantly improved the elevated-temperature mechanical properties [9,11]. Considering the close chemical homology between Ti and Zr [10] and the observed segregating tendency of Ti toward  $\theta'/\alpha$ -Al interfaces [44], it is plausible that the improved stability of the  $\theta'$  precipitates in the 206-L alloy after the 300°C/1000h exposure

in the present study was associated with the excess content of Ti that tends to stabilize the  $\theta'$  phase in a manner similar to that of Zr [11,42,45].

These studies [11,24] also demonstrated that through the combined addition of Zr and Mn to a 206-type alloy, the  $\theta'$  precipitates remained resistant to transformation into equilibrium  $\theta$  phase after a 300°C/200h exposure, thus giving the alloy a much higher YS at 300 °C (Table 7). A recent study [13] in our group has shown that the presence of multiple transition elements (Zr, V, and Ti) could greatly improve the thermal stability of  $\theta'$  and thus increase the YS at 300 °C of Al-Cu alloys to a much higher extent (Table 7). Locally anisotropic coarsening of the  $\theta'$  precipitates along the  $\langle 100 \rangle_{\text{Al}}$  directions during the thermal exposure of the 206-L alloy (see Fig. 5) indicates that the efficiency of Ti in retarding the coarsening of  $\theta'$  precipitates was inferior to the combined addition of some transition elements, such as Zr, Mn, Sc, V, and Ti [11,14,15,17,45,46]. The  $\theta'$  precipitates in the Zr/V/Ti-containing Al-Cu 224 alloy exposed at 300 °C for 100–1000 h were almost equal along all two edge-on  $\{200\}_{\text{Al}}$  planes when viewed along the  $\langle 001 \rangle_{\text{Al}}$  zone axis [13]. The inferior efficiency of Ti in retarding the coarsening of  $\theta'$  is also evidenced by the coarsening of the  $\theta'$  precipitates that proceeded through both lengthening and thickening in the 206-L alloy (Table 5). In contrast, the  $\theta'$  precipitates in the Zr/V/Ti-containing Al-Cu 224 alloy [13] solely showed lengthening-dominated coarsening and no thickening during long-term thermal exposure. This could explain why the 206-L alloy displayed the continuing decline in YS with prolonged thermal exposure, but the YS remained constant at the high level of ~120 MPa in the Zr/V/Ti-containing Al-Cu 224 alloy during thermal exposure at 300 °C up to 1000 h [13].

In addition, although it had the same high Ti concentration, the majority of  $\theta'$  precipitates in the 206-H alloy transformed into equilibrium  $\theta$  phase after the 300°C/100h exposure (Fig. 6), indicating much lower stability of  $\theta'$  phase in this alloy than in the 206-L alloy. This is thought to be associated with the higher concentration of Si in the 206-H alloy compared to the 206-L alloy (see Table 1). The kinetics of the  $\theta'$  to  $\theta$  transformation have been found to accelerate in Al-Si-Cu foundry alloys containing 7–9% Si due to the deleterious influence of Si on the stability of the  $\theta'$  phase [18-20,42], although the mechanism behind this effect remains unknown. Studies on Al-Cu alloys have revealed that Si substitutes on Cu lattice sites in the  $\theta'$  phase [21], and the content or solubility of Si in this phase substantially decreases with increasing temperature [21]. Hence, the exposure of the 206-H alloy at 300 °C could cause segregation of some Si from the  $\theta'$  phase toward the  $\alpha$ -Al matrix. It might be possible that the segregation of Si from the  $\theta'$  phase and fast diffusivity of Si in the  $\alpha$ -Al matrix facilitate the transformation of  $\theta'$  into equilibrium  $\theta$  phase. The 206-H alloy also contained more Mn (0.3 wt.%), but this element has been found to possess a stabilizing effect on the  $\theta'$  phase via its segregation to  $\theta'$ -Al<sub>2</sub>Cu/ $\alpha$ -Al interfaces [11,45]. It is thus worth remarking that the deleterious influence of 0.3 wt.% Si on the stability of  $\theta'$  precipitates overcomes the beneficial effect of the transition elements, such as Ti and Mn. Therefore, effective control of the thermal stability of the  $\theta'$  phase in Al-Cu alloys also requires accurate control of the Si concentration or the possibility of neutralizing its deleterious influence.

#### 4. Conclusions

The present study focused on the effects of compositional variation of Al-Cu 206 alloys (Si and Mn concentrations, 0.12 wt.% each vs. 0.3 wt.% each) on the thermal stability of  $\theta'$  precipitates and elevated-temperature strengths during long-term thermal exposure at 300 °C. The following conclusions can be drawn.

- Both Al-Cu 206 alloys under the T7 condition exhibited comparable room/elevated-temperature strengths, which were predominantly controlled by the  $\theta'$  precipitates. The alloy with more Si and Mn possessed slightly higher strength due to the co-existence of major  $\theta'$  and minor  $\beta''$  precipitates.
- The  $\theta'$  precipitates in the alloy with low Si and Mn concentrations remained stable and resistant to transformation into the equilibrium  $\theta$  phase during thermal exposure at 300 °C for up to 1000 h, while the alloy with high Si and Mn concentrations experienced an almost complete transformation of  $\theta'$  to  $\theta$  after only 100 h of exposure at 300 °C.

- The  $\theta'$  precipitates observed equally along with all  $\langle 001 \rangle_{Al}$  directions under the T7 condition in the alloy with low Si and Mn concentrations underwent locally anisotropic coarsening along the  $\langle 001 \rangle_{Al}$  directions during thermal exposure. Moreover, coarsening after prolonged exposure proceeded with both lengthening and thickening, resulting in the continuing decline in the YS from 93 MPa after the 300°C/100h exposure to 78 MPa after the 300°C/1000h exposure.
- The instability of the  $\theta'$  precipitates and accelerated transformation to the deleterious  $\theta$  phase during thermal exposure in the alloy with high Si and Mn concentrations gave it a significantly lower elevated-temperature YS (69 MPa after the 300°C/100h exposure and 64 MPa after the 300°C/1000h exposure).
- By comparing both alloys and with other similar Al-Cu alloys, the impacts of Si and Ti on the thermal stability of  $\theta'$  precipitates were explored. The key role of the combined addition of transition elements on improving  $\theta'$  stability and the strategic design of Al-Cu alloys for high-temperature applications were highlighted.

## Acknowledgements

The authors would like to acknowledge the financial support of the Natural Sciences and Engineering Research Council of Canada (NSERC) under the Grant No. CRDPJ 514651-17 and Rio Tinto Aluminum through the Research Chair in the Metallurgy of Aluminum Transformation at University of Quebec in Chicoutimi.

## References

1. T. Dorin, M. Ramajayam, J. Lamb, T. Langan, Effect of Sc and Zr additions on the microstructure/strength of Al-Cu binary alloys, *Materials Science and Engineering: A*, 2017, **707**, p 58-64
2. M. Javidani, D. Larouche, Application of cast Al-Si alloys in internal combustion engine components, *Int. Mater. Rev.*, 2014, **59**(3), p 132-158
3. J. Rakhmonov, G. Timelli, F. Bonollo, The Effect of Transition Elements on High-Temperature Mechanical Properties of AlSi Foundry Alloys A Review, *Adv. Eng. Mater.*, 2016, **18**(7), p 1096-1105
4. A.R. Farkoosh, M. Pekguleryuz, Enhanced mechanical properties of an Al-Si-Cu-Mg alloy at 300 degrees C: Effects of Mg and the Q-precipitate phase, *Mater. Sci. Eng., A*, 2015, **621**, p 277-286
5. L. Jin, K. Liu, X.G. Chen, Evolution of dispersoids and their effects on elevated-temperature strength and creep resistance in Al-Si-Cu 319 cast alloys with Mn and Mo additions, *Materials Science and Engineering: A*, 2020, **770**, p 138554
6. S. Bai, X.W. Zhou, Z.Y. Liu, P. Xia, M. Liu, S.M. Zeng, Effects of Ag variations on the microstructures and mechanical properties of Al-Cu-Mg alloys at elevated temperatures, *Mater. Sci. Eng., A*, 2014, **611**, p 69-76
7. A. Biswas, D. Sen, S.K. Sarkar, Sarita, S. Mazumder, D.N. Seidman, Temporal evolution of coherent precipitates in an aluminum alloy W319: A correlative anisotropic small angle X-ray scattering, transmission electron microscopy and atom-probe tomography study, *Acta Mater.*, 2016, **116**, p 219-230
8. C. Sigli, F. De Geuser, A. Deschamps, J. Lepinoux, M. Perez, Recent advances in the metallurgy of aluminum alloys. Part II: Age hardening, *Cr Phys*, 2018, **19**(8), p 688-709
9. B. Rouxel, M. Ramajayam, T.J. Langan, J. Lamb, P.G. Sanders, T. Dorin, Effect of dislocations, Al<sub>3</sub>(Sc,Zr) distribution and ageing temperature on  $\theta'$  precipitation in Al-Cu-(Sc)-(Zr) alloys, *Materialia*, 2020, **9**, p 100610
10. D. Shin, A. Shyam, S. Lee, Y. Yamamoto, J.A. Haynes, Solute segregation at the Al/ $\theta'$ -Al<sub>2</sub>Cu interface in Al-Cu alloys, *Acta Mater.*, 2017, **141**, p 327-340
11. A. Shyam, S. Roy, D. Shin, J.D. Poplawsky, L.F. Allard, Y. Yamamoto, J.R. Morris, B. Mazumder, J.C. Idrobo, A. Rodriguez, T.R. Watkins, J.A. Haynes, Elevated temperature microstructural stability in cast AlCuMnZr alloys through solute segregation, *Materials Science and Engineering: A*, 2019, **765**, p 138279

12. S. Mondol, S.K. Makineni, S. Kumar, K. Chattopadhyay, Enhancement of High Temperature Strength of 2219 Alloys Through Small Additions of Nb and Zr and a Novel Heat Treatment, *Metall. Mater. Trans. A*, 2018, **49A**(7), p 3047-3057
13. J. Rakhmonov, K. Liu, L. Pan, F. Breton, X.G. Chen, Enhanced mechanical properties of high-temperature-resistant Al–Cu cast alloy by microalloying with Mg, *J. Alloys Compd.*, 2020, **827**, p 154305
14. Y.H. Gao, L.F. Cao, J. Kuang, J.Y. Zhang, G. Liu, J. Sun, Assembling dual precipitates to improve high-temperature resistance of multi-microalloyed Al–Cu alloys, *J. Alloys Compd.*, 2020, **822**, p 153629
15. Y.H. Gao, L.F. Cao, C. Yang, J.Y. Zhang, G. Liu, J. Sun, Co-stabilization of  $\theta'$ -Al<sub>2</sub>Cu and Al<sub>3</sub>Sc precipitates in Sc-microalloyed Al–Cu alloy with enhanced creep resistance, *Materials Today Nano*, 2019, **6**, p 100035
16. S.S. Liang, S.P. Wen, X.L. Wu, H. Huang, K.Y. Gao, Z.R. Nie, The synergetic effect of Si and Sc on the thermal stability of the precipitates in AlCuMg alloy, *Materials Science and Engineering: A*, 2020, **783**, p 139319
17. S. Mondol, S. Kumar, K. Chattopadhyay, Effect of thermo-mechanical treatment on microstructure and tensile properties of 2219ScMg alloy, *Materials Science and Engineering: A*, 2019, **759**, p 583-593
18. P. Shower, S. Roy, C.S. Hawkins, A. Shyam, The effects of microstructural stability on the compressive response of two cast aluminum alloys up to 300°C, *Materials Science and Engineering: A*, 2017, **700**, p 519-529
19. P. Heugue, D. Larouche, F. Breton, R. Martinez, X.G. Chen, PRECIPITATION KINETICS OF AN AlSi7Cu3.5Mg0.1 ALLOY WITH Zr AND V ADDITIONS, 16th International Aluminum Alloys Conference, 2018
20. T.K. Akopyan, N.A. Belov, N.V. Letyagin, Effect of Trace Addition of Sn on the Precipitation Hardening in Al–Si–Cu Eutectic Alloy, *JOM*, 2019, **71**(5), p 1768-1775
21. A. Biswas, D.J. Siegel, C. Wolverton, D.N. Seidman, Precipitates in Al–Cu alloys revisited: Atom-probe tomographic experiments and first-principles calculations of compositional evolution and interfacial segregation, *Acta Mater.*, 2011, **59**(15), p 6187-6204
22. A. Lemieux, J. Langlais, X.G. Chen, Reduction of Hot Tearing of Cast Semi-Solid 206 Alloys, *Solid State Phenomena*, 2013, **192-193**, p 101-106
23. K. Liu, X. Cao, X.G. Chen, Tensile Properties of Al–Cu 206 Cast Alloys with Various Iron Contents, *Metall and Mat Trans A*, 2014, **45**(5), p 2498-2507
24. B.K. Milligan, S. Roy, C.S. Hawkins, L.F. Allard, A. Shyam, Impact of microstructural stability on the creep behavior of cast Al–Cu alloys, *Materials Science and Engineering: A*, 2020, **772**, p 138697
25. F. Lotter, D. Petschke, T.E.M. Staab, U. Rohrmann, T. Schubert, G. SEXTL, B. Kieback, The Influence of Trace Elements (In, Sn) on the Hardening Process of Al–Cu Alloys, *Phys Status Solidi A*, 2018, **215**(11),
26. M. Zamani, S. Toschi, A. Morri, L. Ceschini, S. Seifeddine, Optimisation of heat treatment of Al–Cu–(Mg–Ag) cast alloys, *J. Therm. Anal. Calorim.*, 2020, **139**(6), p 3427-3440
27. Y.J. Li, L. Arnberg, Quantitative study on the precipitation behavior of dispersoids in DC-cast AA3003 alloy during heating and homogenization, *Acta Mater.*, 2003, **51**(12), p 3415-3428
28. R. Ivanov, A. Deschamps, F. De Geuser, Clustering kinetics during natural ageing of Al–Cu based alloys with (Mg, Li) additions, *Acta Mater.*, 2018, **157**, p 186-195
29. M.J. Starink, N. Gao, J.L. Yan, The origins of room temperature hardening of Al–Cu–Mg alloys, *Materials Science and Engineering: A*, 2004, **387-389**, p 222-226
30. Z. Shen, Q. Ding, C. Liu, J. Wang, H. Tian, J. Li, Z. Zhang, Atomic-scale mechanism of the  $\theta'' \rightarrow \theta'$  phase transformation in Al–Cu alloys, *Journal of Materials Science & Technology*, 2017, **33**(10), p 1159-1164
31. I.C. Barlow, W.M. Rainforth, H. Jones, The role of silicon in the formation of the (Al<sub>5</sub>Cu<sub>6</sub>Mg<sub>2</sub>)  $\sigma$  phase in Al–Cu–Mg alloys, *J. Mater. Sci.*, 2000, **35**(6), p 1413-1418
32. S. Roy, L.F. Allard, A. Rodriguez, W.D. Porter, A. Shyam, Comparative Evaluation of Cast Aluminum Alloys for Automotive Cylinder Heads: Part II–Mechanical and Thermal Properties, *Metall. Mater. Trans. A*, 2017, **48A**(5), p 2543-2562
33. G.A. Edwards, K. Stiller, G.L. Dunlop, M.J. Couper, The precipitation sequence in Al–Mg–Si alloys, *Acta Mater.*, 1998, **46**(11), p 3893-3904
34. S.J. Andersen, C.D. Marioara, J. Friis, S. Wenner, R. Holmestad, Precipitates in aluminium alloys, *Advances in Physics: X*, 2018, **3**(1), p 1479984

35. S.P. Ringer, B.T. Sofyan, K.S. Prasad, G.C. Quan, Precipitation reactions in Al-4.0Cu-0.3Mg (wt.%) alloy, *Acta Mater.*, 2008, **56**(9), p 2147-2160
36. E. Rincon, H.F. Lopez, M.M. Cisneros, H. Mancha, Temperature effects on the tensile properties of cast and heat treated aluminum alloy A319, *Mater. Sci. Eng., A*, 2009, **519**(1-2), p 128-140
37. J.F. Nie, B.C. Muddle, Microstructural design of high-strength aluminum alloys, *J Phase Equilib*, 1998, **19**(6), p 543-551
38. V. Vaithyanathan, C. Wolverton, L.Q. Chen, Multiscale modeling of theta ' precipitation in Al-Cu binary alloys, *Acta Mater.*, 2004, **52**(10), p 2973-2987
39. V. Vaithyanathan, C. Wolverton, L.Q. Chen, Multiscale modeling of  $\theta'$  precipitation in Al-Cu binary alloys, *Acta Mater.*, 2004, **52**(10), p 2973-2987
40. C.S. Jayanth, P. Nash, Factors affecting particle-coarsening kinetics and size distribution, *J. Mater. Sci.*, 1989, **24**(9), p 3041-3052
41. J.D. Boyd, R.B. Nicholson, The coarsening behaviour of  $\theta''$  and  $\theta'$  precipitates in two Al-Cu alloys, *Acta Metall.*, 1971, **19**(12), p 1379-1391
42. P. Shower, J.R. Morris, D. Shin, B. Radhakrishnan, L.F. Allard, A. Shyam, Temperature-dependent stability of  $\theta'$ -Al<sub>2</sub>Cu precipitates investigated with phase field simulations and experiments, *Materialia*, 2019, **5**, p 100185
43. P. Heugue, D. Larouche, F. Breton, R. Martinez, X.G. Chen, Evaluation of the Growth Kinetics of theta ' and theta-Al<sub>2</sub>Cu Precipitates in a Binary Al-3.5 Wt Pct Cu Alloy, *Metall. Mater. Trans. A*, 2019, **50A**(7), p 3048-3060
44. J.D. Poplawsky, B.K. Milligan, L.F. Allard, D. Shin, P. Shower, M.F. Chisholm, A. Shyam, The synergistic role of Mn and Zr/Ti in producing  $\theta'$ /L12 co-precipitates in Al-Cu alloys, *Acta Mater.*, 2020, **194**, p 577-586
45. P. Shower, J. Morris, D. Shin, B. Radhakrishnan, J. Poplawsky, A. Shyam, Mechanisms for stabilizing  $\theta'$ (Al<sub>2</sub>Cu) precipitates at elevated temperatures investigated with phase field modeling, *Materialia*, 2019, **6**, p 100335
46. S. Mondol, T. Alam, R. Banerjee, S. Kumar, K. Chattopadhyay, Development of a high temperature high strength Al alloy by addition of small amounts of Sc and Mg to 2219 alloy, *Materials Science and Engineering: A*, 2017, **687**, p 221-231

**List of tables:**

Table 1. Chemical composition of experimental alloys (wt.%).

Alloys	Cu	Si	Mn	Mg	Fe	Ti	Al
206-L	4.64	<b>0.12</b>	<b>0.12</b>	0.27	0.14	0.21	Bal.
206-H	4.61	<b>0.29</b>	<b>0.32</b>	0.29	0.16	0.21	Bal.

Table 2. Types of stable phases and the solute concentration of experimental alloys, which are predicted by thermodynamic equilibrium analysis at 520 °C using Thermo-Calc software.

Alloy	Stable phases	Composition of $\alpha$ -Al matrix, wt. %				
		Cu	Mg	Si	Mn	Al
206-L	$\alpha$ -Al, Al <sub>7</sub> Cu <sub>2</sub> Fe	4.37	0.27	0.12	0.12	Bal.
206-H	$\alpha$ -Al, Al(FeMn)Si and Al <sub>2</sub> Cu	4.47	0.29	0.19	0.11	Bal.

Table 3. Electrical conductivity and microhardness of the two alloys after solution treatment.

Alloy	EC, % IACS	Microhardness, HV
206-L	31.57	116.2
206-H	29.86	118.4

Table 3. Quantitative TEM results of the  $\theta'$  phase in the experimental alloys under the T7 condition.

Alloy	Length, $\mu\text{m}$	Thickness, $\mu\text{m}$	Number density, $\mu\text{m}^{-2}$
206-L	0.0460 ( $\pm 0.011$ )	0.0036 ( $\pm 0.0006$ )	2197
206-H	0.0550 ( $\pm 0.020$ )	0.0039 ( $\pm 0.0008$ )	1812

Table 4. TEM-EDS results of the  $\sigma$ -Al<sub>5</sub>Cu<sub>6</sub>Mg<sub>2</sub> phase (1) and the matrix (2) shown in Fig. 3a.

Analyzed phases	EDS results (wt.%)					
	Cu	Mg	Si	Mn	Ti	Al
$\sigma$ -Al <sub>5</sub> Cu <sub>6</sub> Mg <sub>2</sub>	16.44	2.18	-	0.07	0.1	81.20
$\alpha$ -Al	2.90	0.32	-	0.08	0.28	96.44

Table 5. Quantitative TEM results of the  $\theta'$  phase in the 206-L alloy after exposure at 300 °C.

Exposure time	Length, $\mu\text{m}$	Thickness, $\mu\text{m}$
100 h	0.192 ( $\pm 0.097$ )	0.0153 ( $\pm 0.0048$ )

1000 h	0.2059 (±0.089)	0.0185 (±0.0104)
--------	--------------------	---------------------

Table 6. TEM-EDS results of the  $\theta$ -Al<sub>2</sub>Cu (1), S-Al<sub>2</sub>CuMg (2),  $\beta$ -Mg<sub>2</sub>Si (3), and  $\alpha$ -Al matrix (4) shown in Fig. 3a.

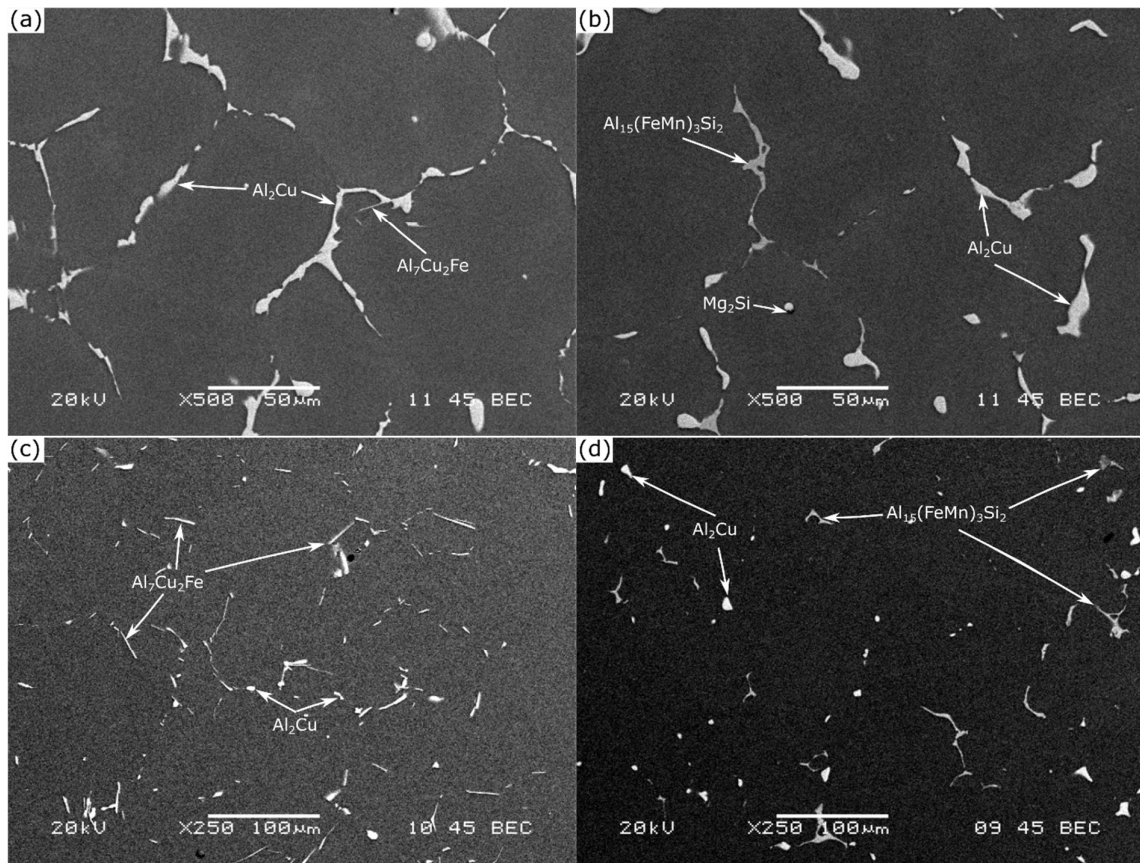
Analyzed phases	EDS results (wt.%)				
	Cu	Mg	Si	Mn	Al
$\theta$ -Al <sub>2</sub> Cu	30.7	-	-	-	69.1
S-Al <sub>2</sub> CuMg	22.1	9.3	5.7	0.8	62.0
$\beta$ -Mg <sub>2</sub> Si	0.2	14.5	6.3	0.4	78.4
$\alpha$ -Al	1.8	0.08	0.02	0.07	97.9

Table 7. Comparison of the elevated-temperature YSs of various Al-Cu cast alloys.

#	Alloys	YS at 300 °C			Reference
		100/200 h	500 h	1000 h	
1	206-L	93	86	78	Present study
2	Al5CuMg (206) -T7	60 *		--	[11,24]
3	Al5CuMnZr-T7	105 *		--	[11,24]
4	Al5CuMgZrVTi (224)	142	125	125	[13]

Note: \* - the thermal exposure condition of these materials is 300°C/200h [11,24].

**List of figures and their captions:**



**Fig. 1.** Optical micrographs showing the typical as-cast (a, b) and solutionized (c, d) microstructures of the 206-L (a, c) and 206-H (b, d) alloys.

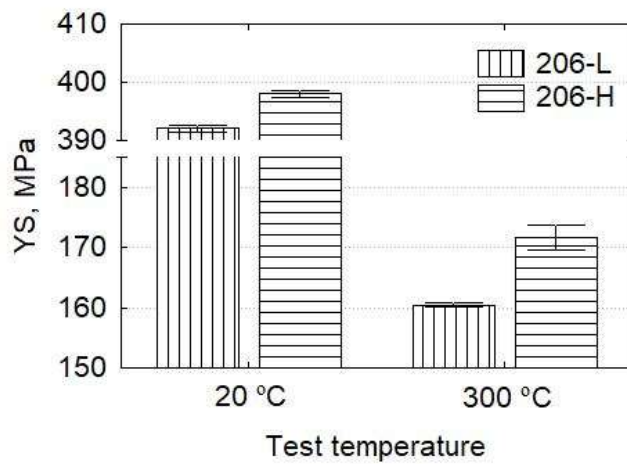


**Fig. 2.** Compressive YSs of the experimental alloys in the T7 state tested at 20 and 300 °C.

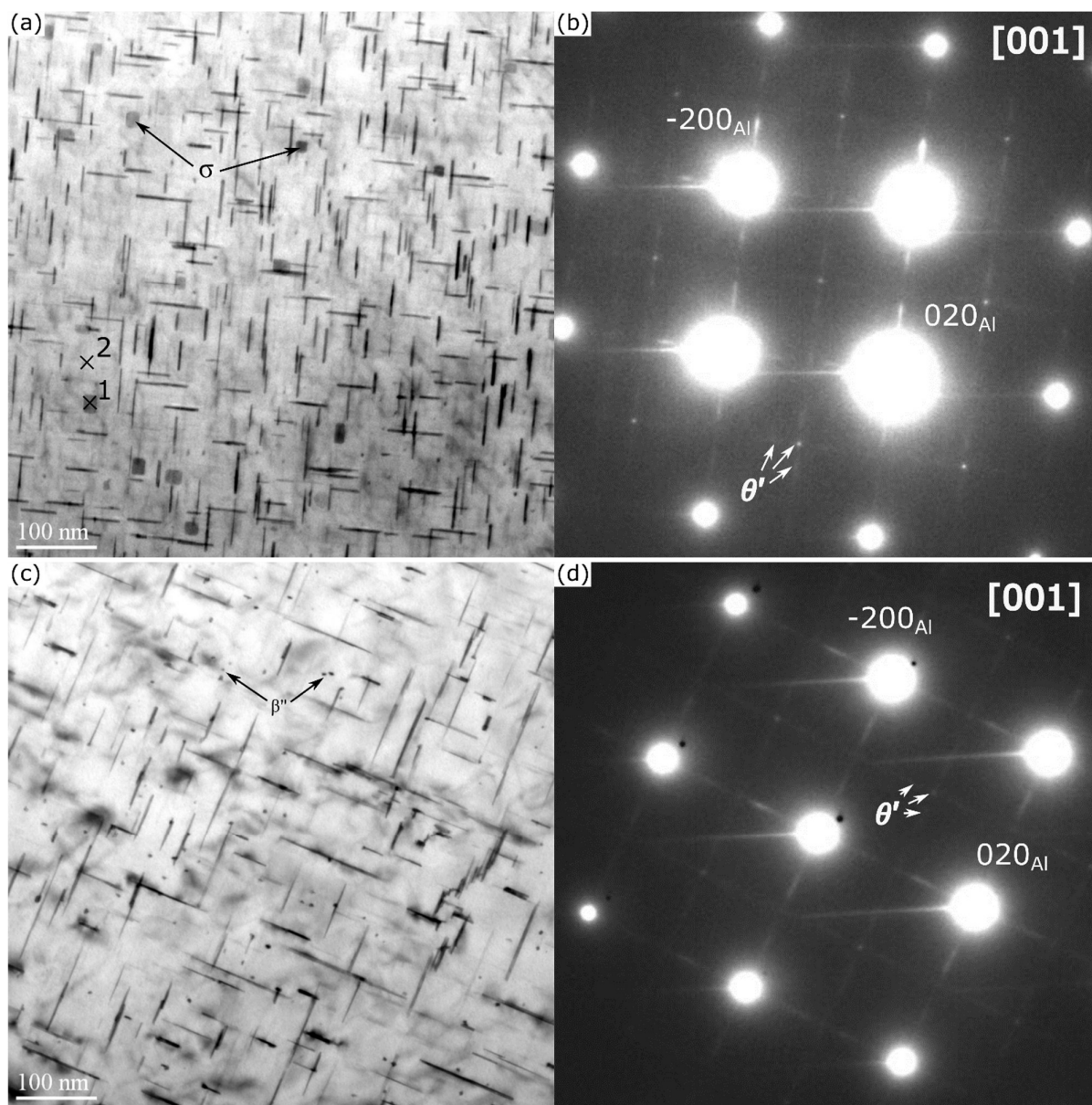


**Fig. 3.** TEM images (a, c) and corresponding SADP (b, d) from the (a, b) 206-L and (c, d) 206-H alloys under the T7 condition. The cross-marks numbered 1 and 2 in **Fig. 3a** indicate where the TEM-EDS analyses were performed.

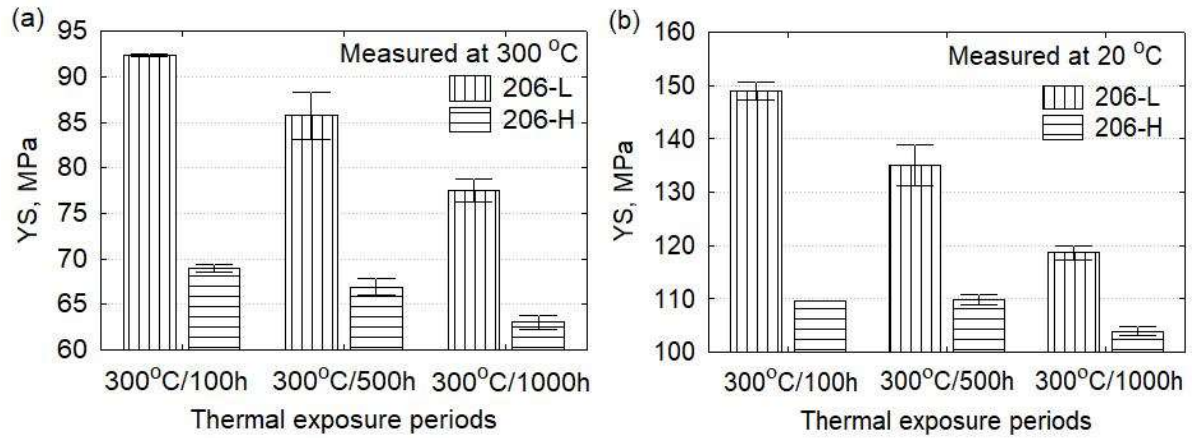


**Fig. 4.** Compressive YSs of the experimental alloys at (a) 300 °C and (b) 20 °C after exposure at 300 °C for various times.

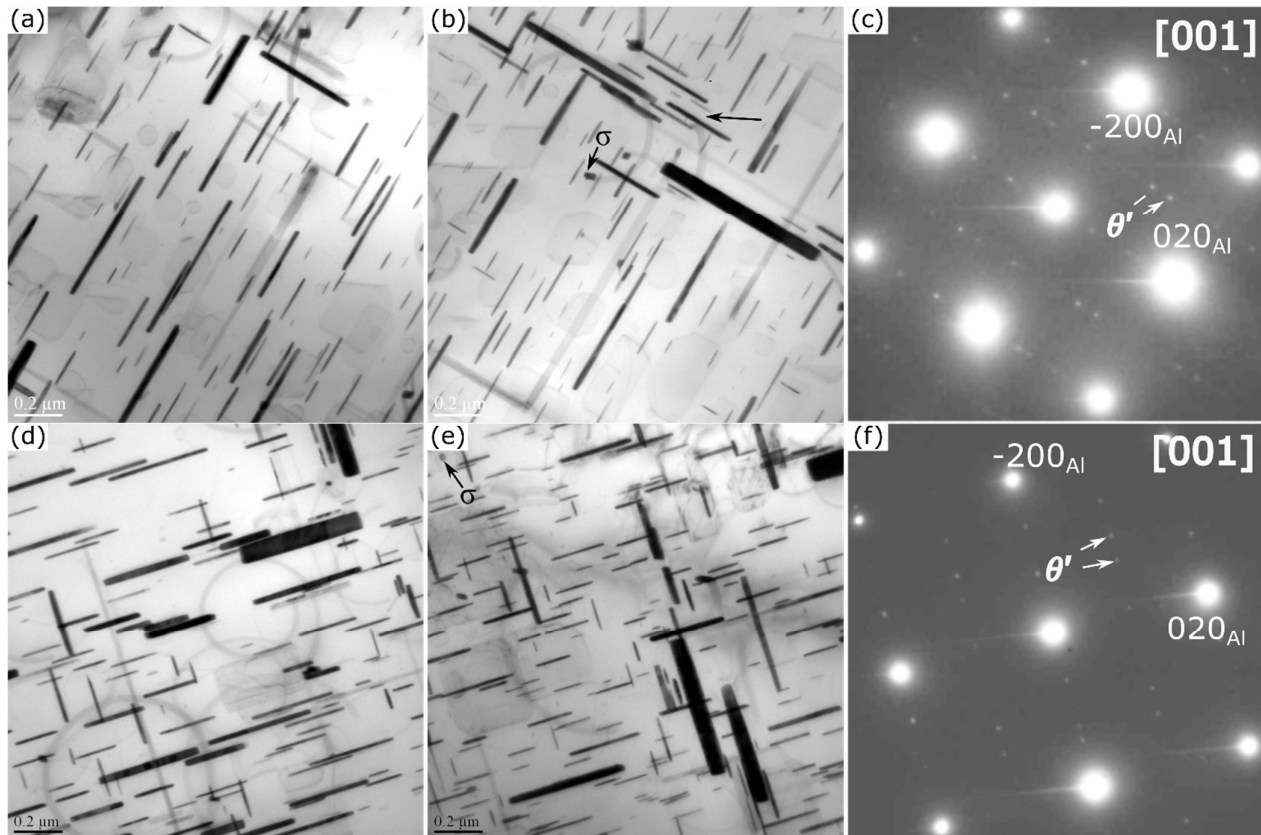


**Fig. 5.** TEM images (a, b, d, e) and corresponding SADPs (c, f) of the 206-L alloy after 300°C/100h (a, b, c) and 300°C/1000h (d, e, f) exposures.

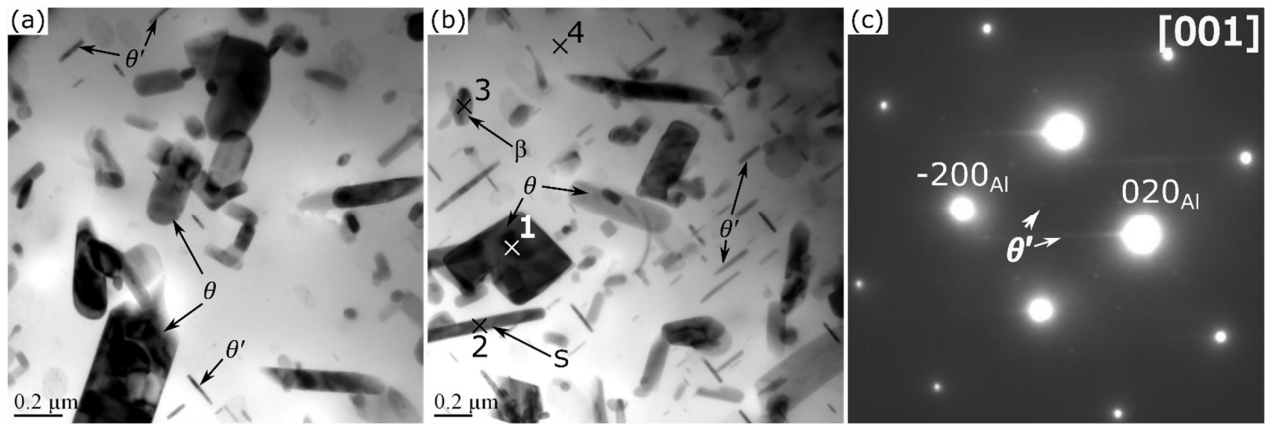


**Fig. 6.** TEM images (a, b) and the corresponding SADP (c) of the 206-H alloy after the  $300^\circ\text{C}/100\text{h}$  exposure. The cross-marks numbered 1, 2, 3, and 4 in Fig. 6b indicate where the TEM-EDS analyses were performed.